Dynamic modelling of an ultra high temperature PCM with combined heat and electricity production for application at residential buildings

I. Violidakis[a], M. Zeneli[a,b], K. Atsonios[a,*], G. Strotos[c], N. Nikolopoulos[a], S. Karellas[b]

[a] Centre for Research and Technology Hellas, Chemical Process & Energy Resources Institute (CERTH/CPERI). Athens branch: Egialias 52, GR 15125 Marousi, Athens, Greece
[b] Laboratory of Steam Boilers and Thermal Plants National Technical University of Athens, 9, Heroon Polytechniou Street 15780, Zografou, Greece
[c] University of Thessaly, GR 41110 Larissa, Greece

ARTICLE INFO

ABSTRACT

The present study investigates the thermal performance of an ultra-high temperature (> 1000 °C) latent heat thermal energy storage system that utilizes silicon as a phase-change (PCM) material. Application of this system in the residential sector is studied, when integrated with a solar PV as an energy source and a hybrid thermionic-photovoltaic (TIPV) converter to produce both electricity and heat and subsequently cover corresponding domestic demand. A one-dimensional (1D) dynamic model has been developed in Dymola modelling tool for predicting the temperature profile and total charging and discharging time of the PCM heat storage system, as well as the produced thermal and electric power from the hybrid TIPV converter. A sensitivity analysis both for the melting and the solidification stage of the PCM has been performed based on key parameters, such as material thermal properties –including specific heat capacity, thermal conductivity and latent heat of fusion- and other operating and design parameters. The results have showed an increasing linear dependence of charging and discharging time on specific heat, latent heat of fusion and density and a decreasing dependence on thermal conductivity. Finally, the integration of the heat storage system on a building level has showed the potential for high coverage of either heat demand (over 100%) or electricity demand (over 69%) for a typical Southern European household, depending on the generation priority strategy followed.

1. Introduction

The household energy demands are growing at a fast pace worldwide. In fact, the residential sector accounted for more than 25% of the EU-28 total final energy consumption in 2015, being the third energy consuming sector after transport and industry [1]. A substantial amount of the total energy used in the residential buildings is associated with space heating and cooling, accounting for 50% of the total consumptions [2]. In EU households, heating and hot water alone account for 79% of total final energy use. Currently, only 16% of heating and cooling is generated from renewable energy sources (RES), making decarburization of the heating and cooling sector essential in order to reach and fulfil the EU's climate and energy goals.

Towards this direction, several RES based schemes have been proposed for renewable heating and cooling that are either on a research or in a commercial scale. Among them, strategies based on combination of photovoltaic (PV) power with electricity-driven air conditioning equipment, mainly heat pumps, attract the interest of several studies [3–8]. These investigations focus on optimizing use and management of thermal energy by allowing it to be stored to level demand peaks, increasing use of renewables affected by intermittency, such as solar-based heating [9]. Most of the proposed technological solutions for energy storage include either batteries (BESS) or Thermal Energy Storage (TES) systems. The latter one offers an increase in overall efficiency and better reliability, when applied in advanced energy systems, leading to better economics, reductions in investment and running costs, as well as reductions in carbon dioxide (CO_2) emissions [10]. However, most current systems are water-based, and their storage capacity depends on the operating temperature difference of the heating system used.

A proposed alternative is latent heat thermal energy storage systems (LHTES) that use Phase Change Materials (PCM) enclosed inside ceramic containers. Those systems have the advantage of storing heat compactly in a narrow temperature range and offer a considerably higher energy density compared to water-based sensible heat storage systems [11]. The effect of using PCMs in solar thermal storage systems has been investigated both in exper-

Nomenclature

c_p, $J \cdot kg^{-1} \cdot K^{-1}$	specific heat capacity
D, m	diameter
E_a, $kWh \cdot m^{-2} \cdot a^{-1}$	total annual energy consumption
H, mm	height
k, $W \cdot m^{-1} \cdot K^{-1}$	thermal conductivity
L, $kJ \cdot kg^{-1}$	latent heat of fusion
Q, $W \cdot cm^{-2}$	input thermal heat flux
R, $K \cdot W^{-1}$	thermal resistance
T, °C	temperature

Greek letters

β, [-]	Liquid fraction
ρ, $kg \cdot m^{-3}$	density

Indexes

abs	absorber
b	base
em	emitter
i	hourly
l, liquidus	liquid state
ref	reference point
s, solidus	solid state
w	wall

Abbreviations

HDH	heating degree-hours
ITC	inverted truncated cone
LHTES	latent heat thermal energy storage
PCM	phase change material
UHT	ultra-high temperature
TIPV	thermionic-photovoltaic
TPV, PV	thermo-photovoltaic, photovoltaic

imental and numerical studies. A demonstration of passive solar energy storage in test cabins with a new microencapsulated bio-based PCM has been recently presented by Cellat et al. [12]. Malan et al. [13] performed a numerical study using Explicit Euler method to analyze the use of solar thermal energy storage with heat pipes and fins for improved heat transfer in a power generation cycle. Grange et al. [14] applied the implicit forward method in time and upwind difference scheme in space for simulating the thermal energy storage system in order to study the effect of its use on the performance of hybrid solar gas-turbine plant. Belmonte et al. [15] studied a solar system with PCM fluidized bed energy storage for building heating, using equations proposed by Izquierdo-Barrientos et al. [16] in an algorithm written in MATLAB software. Parsazadeh et al. [17] used a CFD model to simulate melting of nanoparticle-enhanced PCM in a shell and tube thermal energy storage through the enthalpy-porosity approach. Kant et al. [18] studied a thermal energy storage system with PCM and fatty acid nanoparticle, using COMSOL software for solving partial differential equations.

However, utilization of LHTES systems is currently restricted in terms of operation, from low to medium temperatures (<1000 °C) [19,20] which, in turn, restrict the system operating range and efficiency. Furthermore, the vast majority of commercial PCMs, such as salt hydrates, paraffins, and eutectic water-salt solutions [21], have low thermal conductivities that lead to low charging/discharging rates [22]. Storage at ultra-high temperature (>1000 °C) with the utilization of metallic PCMs – of high thermal conductivities and latent heat of fusion- can potentially lead to greater energy densities than the ones achieved in low temperature LHTES systems [23,24]. Recent theoretical and experimental testing has highlighted the importance of using pure silicon or its alloys in those systems [25,26]. Silicon is advantageous, in comparison to molten salts, both in terms of energy density (an order of magnitude higher) and melting temperature (1414°C) [27]. Over and above, the silicon melting temperature matches well the band gap of state-of-the-art thermophotovoltaic cells, allowing, thus, its integration in existing solar-to-heat-to-power (S2H2P) and power-to-heat-to-power (P2H2P) conversion technologies [28].

In this context, ultra-high temperature (UHT) LHTES systems can be used as a heat source for novel heat-to-power converters, such as thermionic converters. In its principal form, such a type of converter consists of two electrodes, i.e. the emitter and the collector, separated at a micron to sub-micron distance and enclosed in a container under vacuum conditions. The efficiency of a thermionic converter is strongly based on the temperature difference between the cathode and the anode. The cathode, usually constructed by a metallic material, should reach ultra-high temperatures (>1000 °C), and, thus, it is connected with a heat source (LHTES system preferably to maintain a constant heat flux). This complies with the thermionic emission, a phenomenon that is negligible at room temperature and is greatly enhanced for temperatures above 1000 °C. The anode, a multi-junction PV cell, should be kept at a temperature as low as possible (lower than 100 °C), and is connected to a heat sink. This is mainly done in order to enhance the collection of the emitted electrons and prevent efficiency decline over the PV cell, due to its overheat. Combining, thus, an ultra-high temperature LHTES and a heat sink with a thermionic photovoltaic (TIPV) electronic converter can boost its conversion efficiency.

TIPV converters include various advantages and seem as an attractive solution to be integrated in power systems. Some of these advantages are the capability to directly convert thermal energy into electricity, the long lifetime due to lack of moving parts and the high efficiency which can theoretically reach 40% or above [29], for cathode temperatures exceeding 1000 °C. This mainly occurs because they take advantage of both the photovoltaic and thermionic emission phenomena, thus increasing the produced power density. Finally, the thermal energy collected by the heat sink can also be effectively used to cover the thermal needs of a building or another installation. Thus, when combined with a LHTES system, as the one studied in this work, they can convert stored heat into both electricity and heat on demand, based on the needs of the electrical grid.

Notwithstanding, research on such ultra-high-temperature LHTES-TIPV systems is at an early stage. It focuses mostly on identifying suitable candidates as PCMs that are tested in a lab-scale [30,31]. In previous work, Datas et al. [32] studied the behavior of thermal storage coupled with solar thermo-photovoltaic system operating in steady state and Veeraragavan et al. [33] performed a theoretical analysis, verified by CFD, of the night time performance of a similar system i.e. a system that integrates thermal storage via phase change materials and thermophotovoltaics for power generation. In recent work [34], a silicon-based latent heat storage system operating at ultra-high temperatures has been investigated by our research team through a validated transient computational fluid dynamics model, which combined the multiphase volume of fluid method with the enthalpy-porosity approach and applied an adaptive local grid refinement technique. However, before such systems are considered as a solution readily available for connection to the power grid in residential sector, further theoretical research and development is required. Several areas should be addressed: (1) Achievement of high-charge discharge rates, (2) selection and design of appropriate LHTES containers, (3) integration of LHTES-TIPV systems to a building level, and (4) use of proper materials of high lifetime and low reactivity.

This study focuses on the first three areas and puts specific attention on the integration of the LHTES-TIPV system on a domestic level to cover electricity and heating needs of a typical Southern European residence. Additionally, a technical assessment of the thermal performance of the UHT-LHTES system during melting and solidification is presented, under varying PCM properties, design parameters and operating conditions. For this purpose, a 1D model is developed in Dymola, a tool for dynamic energy simulations, to calculate the temperature profile and total charging and discharging time of the UHT-LHTES system, as well as the energy produced from the TIPV for covering electricity demand. In the currently studied concept, the indispensable heat extraction (cooling by means of a copper plate heat spreader and water as a coolant) of the PV cell of the hybrid TIPV converter is also exploited to cover the building heat demand. Finally, as a heat source of the UHT-LHTES system, a PV system is used to provide, whenever available, the energy to be used or stored for covering the energy needs. Initially, the applied model is successfully verified against a computational fluid dynamics (CFD) model, which had been validated against experimental data in a previous work [34]. The applied methodology is based on the enthalpy-porosity approach, an implicit method to track the solid-liquid phase change front, originally proposed by Voller et al. [35]. For its numerical solution a common one-dimensional (1D) finite difference method is applied, but with a new reformulation, to take into account vessel shape variation. This new approach is helpful in the analysis by providing a rapid method to parametrically investigate numerous material properties and other parameters of PCMs prospective for application in domestic heat storage. Results of this analysis are of high importance, since the potential of utilizing a demanding –yet advantageous- UHT-LHTES system in a building level, which has been studied only once recently by Datas et al. [36], is successfully demonstrated, by utilizing a simple and accurate numerical tool.

2. Methodology

2.1. LHTES-TIPV system description

The LHTES-TIPV system, which is investigated in this work, comprises a series of interconnected components; a silicon-based LHTES module, a heat-to-electricity solid-state device and a copper plate heat spreader. The heat-to-electricity device, i.e. a hybrid thermionic-photovoltaic (TIPV) converter, consists of two electrodes -a hot emitter and cold collector- separated by an ultra-high vacuum gap. During operation, the TIPV emitter is heated up directly by the PCM container, reaches ultra-high temperatures ($>$1000 °C) and starts emitting photons and electrons towards the TIPV collector. By this manner, high temperature thermal energy is directly converted into electricity. At the TIPV collector rear side, where the PV cell resides, the copper plate heat spreader acts as a heat sink of the excess thermal energy [37,38]. In this type of cooling system, water is used as a coolant. The whole system follows a cycling performance of various charging-discharging periods. During charging period (usually daytime), the PCM vessel stores thermal energy in the form of latent heat. During discharging period, the TIPV device is connected to the LHTES system and converts part of the stored thermal energy into electricity. The remainder is utilized as high enthalpy thermal energy, through the effective heat recovery by the cooling medium. This novel LHTES-TIPV system, due to its compact design, can be easily integrated into a building level to cover electricity and heat demands (Fig. 1).

2.2. Residential building integration

In the proposed configuration (Fig. 1), a PV system uses solar energy to produce electricity, which is then converted through an electric resistor into heat to charge the LHTES. The energy stored in the integrated LHTES is then supplied to a building, giving priority to cover, either the electric or the heat demand first, as deemed appropriate according to the selected strategy.

The input set of data used for this investigation involves heat and electric demand profiles for a typical Southern European residence and the electricity production from a PV system, which covers the corresponding energy needs, when available. The residence location is assumed to be in Southern Europe, since the solar power potential there can be significant for covering a substantial part of the thermal energy needs.

The heat demand has been calculated based on the method of heating degree-hours, which result from the difference ΔT of the hourly environmental temperature, T_i, subtracted from a base temperature, T_b, which in this case is set to be 15.5°C, as it is the standard for the European Union [39], i.e.:

$$\Delta T_i = T_b - T_i \tag{1}$$

It is remarked that in a more case specific analysis, a regional base temperature should be taken into account according to the respective regional regulations.

The total heating degree-hours (HDH) for a year are calculated as the sum of all those differences, when they are positive:

$$HDH = \sum_{i=1}^{N} \Delta T_i^{+}, \tag{2}$$

where N=8760 is the number of total hours per year and the '+' sign indicates that only positive values are taken into account in the sum.

The total annual energy consumption, E_a is calculated based on the energy used for heating per year and square meter ($kWh \cdot m^{-2} \cdot a^{-1}$). According to an online database, taking into account a generic residence in climate Zone B of Greece, built between 2001 and 2010, with a reference floor area of 115 m^2 [40], E_a is specified to be 64.8 $kWh \cdot m^{-2} \cdot a^{-1}$. Therefore, the total annual energy consumption amounts to E_a=64.8 $kWh \cdot m^{-2} \cdot a^{-1} \cdot$ 115 m^2=7452 $kWh \cdot a^{-1}$.

The heat demand per hour has been calculated as the product of the total annual energy consumption multiplied with the fraction of the total degree-days that are required per hour, i.e.:

$$Q_i = E_a \cdot \frac{\Delta T_i}{HDH}, \tag{3}$$

and it is presented in Fig. 15 of the Annex.

A five-month heating period between the 20th of November and the 20th of April is considered, whereas the heating needs the rest of the year are considered negligible.

For the electricity demand, a typical consumption profile [41] of a Southern European residence has been considered, as seen in Fig. 16 of the Annex.

As seen above, the production of electric energy is achieved through a PV which feeds the heating system. The application of such a system in the specific area leads to an annual energy production profile as that of Fig. 17 in the Annex, according to an online tool for providing location-based hourly power output from solar power plants [16]. It is considered that the PV directly covers as much demand as possible and the excess is fed to the heat storage. The excess power production from the PV is shown in Fig. 18 and the remaining electricity demand in Fig. 19.

2.3. Model description

This study presents a 1D dynamic model (Fig. 2), which calculates the temperature profile and total charging and discharging time of the PCM heat storage system, as well as the produced thermal and electric power from the TIPV converter. The model has
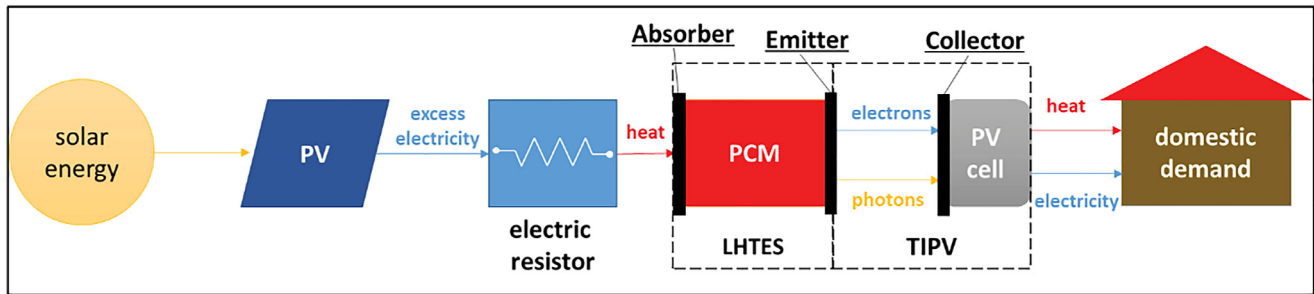
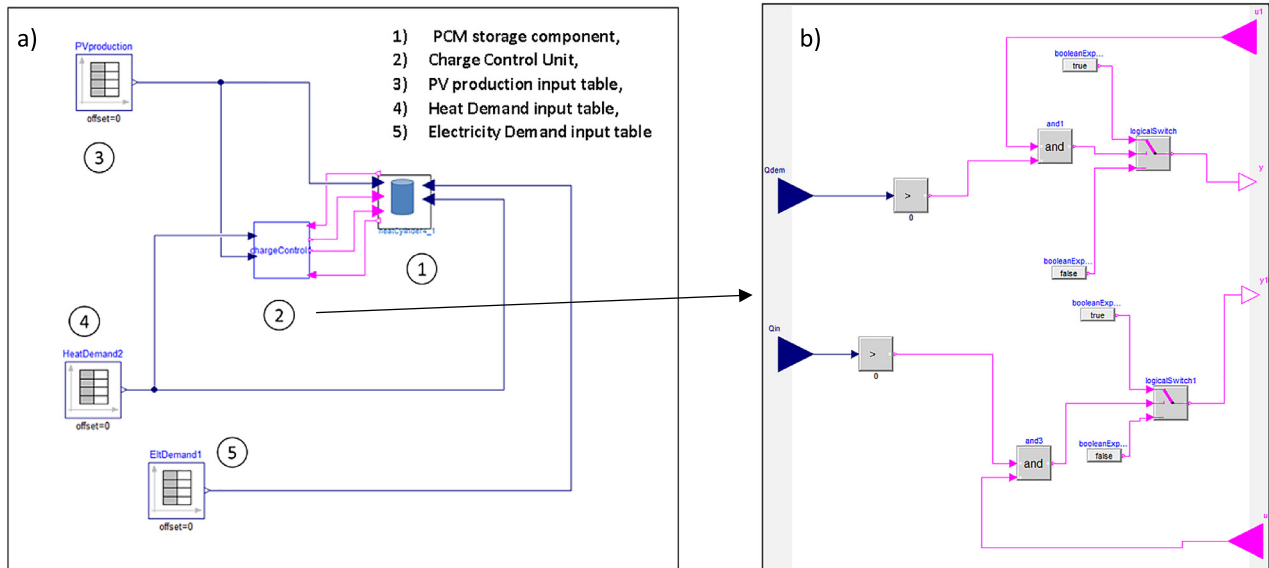**Fig. 1.** Flow chart of the LHTES-TIPV system studied in the present work.

Fig. 2. a) 1D model developed for the LHTES-TIPV converter and b) Charge Control Unit.

been developed in Dymola, a multi-domain tool for dynamic modelling and simulation, which uses the Modelica programming language. The model consists of a main component, developed from scratch, which solves the energy equation and defines the temperature profile of the PCM within the energy storage block and the output of power from the heat-to-electricity device. Another basic component is the charge control unit, which controls the power input and output of the UHT-LHTES system and mainly consists of logical blocks taken from the default Modelica Library. In this model, a PV with installed capacity 5kW$_p$ is employed for providing the UHT-LHTES with heat from electricity.

The simulated cases include two basic geometries, a cylinder and an inverted truncated cone (ITC), as seen in Figs. 3 and 4, which are quite practical to be included in a LHTES system for a building application. In this simulation study, both geometries are considered to be heated from the upper base (absorber surface), when charged, and discharged from the bottom base (emitter surface). As concerns the heat losses from the sidewalls, different scenarios have been studied, which either consider adiabatic walls (ideal conditions), or include heat losses by imposing a thermal resistance value at the walls (realistic conditions).

Fig. 2a) presents a diagram view of the 1D model developed and Fig. 2b) a detailed diagram view of the charge control unit. In the 1D model, the PCM vessel (1) is the main heating storage component, and the charging and discharging phase are determined by the charge control unit (2). The power production from the PV, the heat and electricity demand are imported to the PCM vessel component from the table components (3), (4) and (5) respectively. Two more inputs, which introduce two Boolean vari-

ables that specify when the PCM storage component gets into a charging or discharging phase, are also imported from the charge control unit (2). Finally, two other Boolean variables are also exported, which define whether the PCM material has completely solidified or melted. The charge control unit has those two Boolean variables as input, and also two more inputs for the power production and the heat or electricity demand, depending on the priority strategy selected in each case. Based on these, the charge control unit checks whether there is available power production from the PV. Then, if the PCM is not fully melted (i.e. storage not completely full), it exports an output Boolean variable, specifying that the PCM storage component is in a charging phase. Similarly, the charge control unit checks whether there is a demand (either heat or electricity) and whether the PCM is not completely solid (i.e. storage not completely empty) and if these conditions are met, it exports another output Boolean variable which specifies that the PCM storage component is in a discharging phase.

2.4. Numerical methodology

The applied Dymola 1D model utilizes the enthalpy-porosity approach to simulate the PCM solidification/melting process. This approach, which originates from the work of Voller and Prakash [35], tracks the solid-liquid front implicitly, offering speed-up and convergence stability in the calculations. In this method, the latent heat is accounted in the energy equation, instead of the temperature, whilst it is assumed that the PCM phase change occurs in a temperature range, rather than a single point. Finally, the liquid-solid mushy zone region is treated as a porous medium. In many
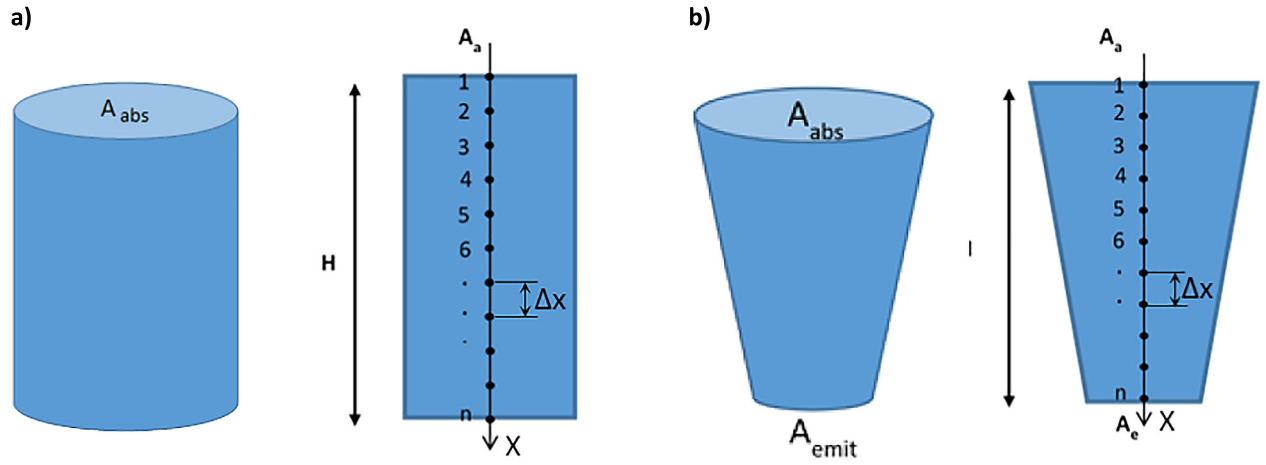
a)

b)

Fig. 3. Geometry and discretization display of the Dymola 1D model for the a) cylinder and b) inversed truncated cone case.
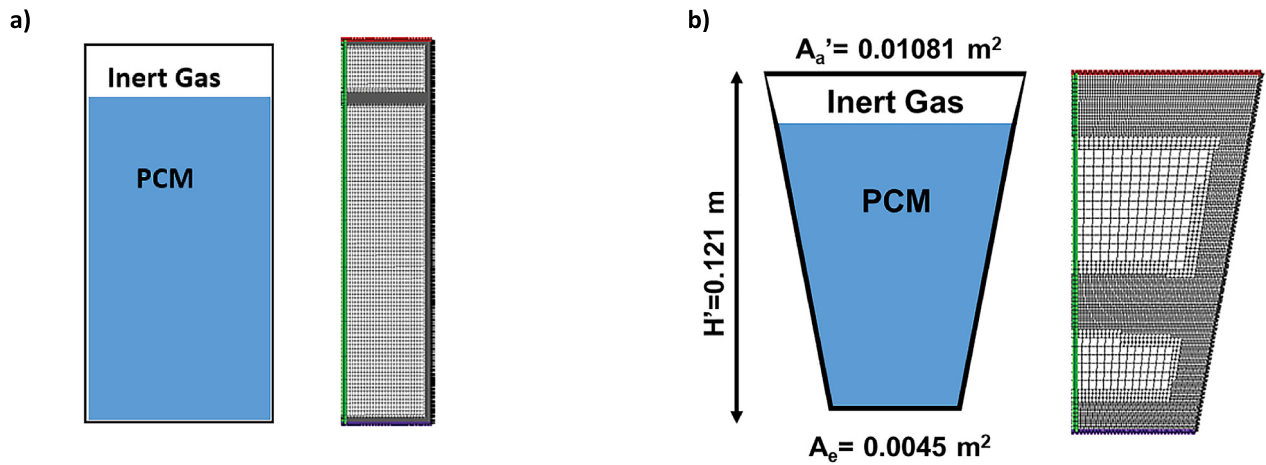
a)

b)

Fig. 4. Geometry and mesh layout of the CFD (axisymmetric) model for the a) cylinder and b) truncated cone case. Purple: emitter surface, green: axis, red: absorber, black: walls [45].

cases, such as metal alloys this mushy region indeed exists. However, in case of pure metals that melt at a single temperature point this assumption is mainly followed from a numerical perspective, since a step change in the PCM liquid fraction and its thermal properties might cause numerical instabilities during calculation.

Some of the assumptions of the 1D enthalpy-porosity model that are applied in the present paper are the following:

1 No fluid flow phenomena are considered during the charging and discharging stage within the vessel, but only heat conduction. Heat transfer through convection is neglected. This is applicable during the PCM solidification phase, where thermal conduction predominates [42,43]. During melting, the effect of buoyancy driven-natural convection greatly depends on the values of Rayleigh and Stefan numbers, the heat source location and heat flux magnitude. High Stefan and Rayleigh numbers and/or position of the heat source at the vessel sidewalls increase the role of natural convection, otherwise, as in the present cases studied, conduction is the major driving force in the PCM melting [44]. Furthermore, heat conduction is highly enhanced owing to silicon's high thermal conductivity, which is almost an order of magnitude higher than the conventional molten-salt based PCMs;

2 The PCM density and thermal conductivity change during its transition from solid to liquid phase and vice versa. Their variation inside the mushy region is linear. Nevertheless, the PCM volumetric change and the floating of the solid phase inside the liquid PCM are not taken into account

3 The vessel is filled exclusively by the PCM – In the real application, the crucible is filled partially by PCM and in its upper part by an inert gas (e.g. argon);

4 The released heat from the vessel bottom part –emitter– during discharging mode is based on an empirical correlation (8) and is prescribed as a boundary condition there;

5 The TIPV emitter comes into direct contact with the PCM.

6 Heat losses from the crucible sidewalls are initially considered negligible in the verification cases, for simplification. In the following case of simulating a full charging and discharging cycle within a 24h period, thermal losses are taken into account by imposing an appropriate thermal resistance at the vessel walls. The latter value has been chosen based on an analysis previously conducted by means of an axisymmetric 2D problem in ANSYS Fluent software [45].

The energy equation is reformulated to take into account the vessel shape that has either the form of a cylinder of a truncated cone:

■ Cylinder

Energy equation in 1D

$$\frac{\partial\left[\rho c_p \cdot (T - T_{ref})\right]}{\partial t} + \Phi = \frac{\partial\left(k \cdot \frac{\partial T}{\partial x}\right)}{\partial x} - Q_{loss} \tag{4}$$

where T is the temperature at a point of the PCM, T_{ref}, the reference temperature (= 25°C or 298.15 K) ρ, the PCM density (kg·m^{-3}), c_p the specific heat capacity (J·kg^{-1}·K^{-1}) and k the thermal conductivity of the PCM (W·m^{-1}·K^{-1}).

■ Inverted Truncated cone:

Fourier equation

$$q = -k \cdot \frac{\partial T}{\partial x} \qquad (5)$$

Energy equation in 1D

$$\frac{\partial \left[\rho c_p \cdot \left(T - T_{ref} \right) \right]}{\partial t} + \Phi = -\frac{\partial (A(x) \cdot q)}{\partial V} - Q_{loss} \qquad (6)$$

where $A(x) = \pi \cdot r^2(x)$ is the cross-section surface at a point, x, along the cone, with r(x) being the radius of the cross-section, and $dV = \frac{1}{3} \pi (r_1^2 + r_1 r_{2+} r_2^2) dx$, a finite truncated cone volume, where r_1, r_2 the radius of the bases of the finite volume.

In both cases $\Phi = \frac{\partial (\rho \cdot \beta L)}{\partial t}$ is a sink term, which expresses the absorbed (released) latent heat of melting (solidification). The liquid fraction β is defined according to the following equation:

$$\beta = \begin{cases} 1 & if \ T > T_{liquidus} \\ \dfrac{T - T_{solidus}}{T_{liquidus} - T_{solidus}} & if \ T_{solidus} < T < T_{liquidus} \\ 0 & if \ T < T_{solidus} \end{cases} \qquad (7)$$

The equation of the heat flux imposed at the emitter surface during discharge is the following:

$$Q_e = -\left(3.17E-04 \cdot T_{em}^3 - 0.7616 \cdot T_{em}^2 \right. $$
$$\left. +6.438E02 \cdot T_{em} - 1.8385E05 \right), \qquad (8)$$

where T_{em} is the emitter temperature. It should be noted that this equation is a 3rd order fit to a simplified radiative/thermionic model that describes the radiative/thermionic exchange, between an emitting surface and a TIPV collector [24,46]. Finally, the equation for heat losses from the heat storage sidewalls, when they are taken into account is:

$$Q_{loss} = A_{walls} \frac{T - Tout}{R} \qquad (9)$$

where A_{walls}, is the corresponding surface section of the sidewalls, T_{out} the ambient temperature and R=1.88 m^{2}K·W^{-1}, the thermal resistance of the walls.

Concerning the heat-to-power device (TIPV converter), additional assumptions are followed in this analysis:

- Between the pair of emitter-collector, ultra-high vacuum conditions are maintained. Therefore, heat transfer through convection between the two electrodes is negligible;
- Radiative and convective heat losses from the sidewalls of the cooling system and the TIPV converter are neglected;
- The thermal energy stored in the form of latent heat in the LHTES module is converted into both electricity and heat at a 32%-68% ratio, according to the electrical conversion efficiency of the TIPV unit [46]. The heat output is totally collected by the coolant and utilized to cover any heat demands.

2.5. Numerical cases examined

In the framework of this analysis, the developed 1D model is utilized to identify the effect of the PCM properties on the heat storage block charge and discharge rates. A parametric investigation is carried out by varying several PCM properties, such as specific heat capacity, thermal conductivity and latent heat of fusion. Additionally, the effect of the vessel geometry on the solidification/melting rates of the contained PCM is also assessed. Later on, the integration of the whole LHTES-TIPV unit on a building level, with a realistic case of covering electricity and heat demands within a 24 h period, is also examined.

Table 1
PCM properties and vessel geometric characteristics.

Parameters	Symbol	Cylinder	Truncated Cone
Thermal conductivity	k	20 W·m^{-1}K^{-1}	20 W·m^{-1}K^{-1}
Specific heat	c_p	1040 J·kg^{-1}·K^{-1}	1040 J·kg^{-1}·K^{-1}
Density	ρ	1 kg·m^{-3}	1 kg·m^{-3}
Absorber surface	A_{abs}	0.0108 m^2	0.0108 m^2
Emitter surface	A_{emit}	0.0108 m^2	0.0045 m^2
Height	H	0.112 m	0.112 m
Melting point	T_l	82°C	82°C
Solidification point	T_s	80°C	80°C
Latent heat of fusion	L	Case Ia 1000 J·kg^{-1}	1000 J·kg^{-1}
		Case Ib 1.8·10^6 J·kg^{-1}	

Table 2
Boundary condition used in Dymola 1D model during PCM solidification.

	BC type	Parameters	Units	Values
Wall	Wall	Q	W·m^{-2}	Q_{losses}
Absorber	Wall	Q	W·m^{-2}	Q'_{losses}
Emitter	Wall	Q	W·m^{-2}	Q_e (T)

Table 3
Boundary conditions used in Dymola 1D during PCM melting.

	BC type	Parameters	Units	Values
Wall	Wall	Q	W·m^{-2}	0
Absorber	Wall	T	K	2000
Emitter	Wall	Q	W·m^{-2}	0

2.5.1. 1D model verification

Initially, the Dymola 1D solidification/melting model is verified against a CFD model, which has been previously validated against experimental data for the solidification/melting process of paraffin wax, RT27, at low temperatures, i.e. melting temperatures almost equal to 303.15 K, inside a spherical container [47]. Similar to the 1D model, the CFD model is based on the enthalpy porosity approach and apart from thermal conduction, the effect of buoyancy-driven natural convection is taken into account in the heat transfer process. It should be noted that validation of the 1D model against experimental data would be preferable, however, is not attainable, due to lack of such a set of data for ultra-high temperatures and for such a type of geometrical configurations.

In the model verification, the melting process has been examined for both geometries, during which they are only considered to be heated from the absorber, while the sidewalls and bottom base are considered adiabatic. During the solidification process, there is no heat input for storage and the already stored energy is discharged from the emitter. This case has also been verified and cross-checked versus previous results from the CFD model, comparing the discharging time.

The geometry used in the 1D and CFD models for the inversed truncated cone and the cylindrical design are depicted in Figs. 3 and 4, respectively. In both models, the vessel geometry is placed vertically.

In the 1D model the sealed crucible includes only the PCM, whilst in the CFD model, the molten PCM fills 85% of the vessel and the rest of the domain is filled with an inert gas. For this purpose, the height H of the crucible in the 1D model matches the height of the molten PCM in the vessel of the CFD simulation. In the Fluent CFD model, the problem is solved as axisymmetric and the adaptive local refinement technique -2 levels of refinement- is implemented in the gas-PCM and solid-liquid PCM interface region. This refinement technique results in a maximum grid size of almost 7000 cells.

Table 4
Material (silicon) properties used in 1D model.

Property	ρ, kg m^{-3}	k, W m^{-1} K^{-1}	C_p, J kg^{-1} K^{-1}	$T_{solidus}$, K	$T_{liquidus}$, K	L, J kg^{-1}
PCM-solid	2330	20	1040	1679	1681	$1.8 \cdot 10^6$
PCM-liquid	Melting	2330	20			
	Solidification	2570	60			

Table 5
List of different dimension cases simulated, during the PCM melting (1D model).

Test Case	Geometry	Dimensions
Case A1	Cylinder	H=0.112 m, A_{abs}=0.0074 m^2
Case A2	Cylinder	H=0.077 m, A_{abs}=0.01081 m^2
Case B	Inverted truncated cone	H=0.112 m, A_{abs}=0.01081 m^2, A_{em}=0.0045 m^2

For the purpose of achieving faster convergence of the CFD Model, in all the verification cases a "virtual" material with a low density (1 kg·m^{-3}) is used.

The following two cases are examined for the cylinder geometry:

- Case Ia with a low value of latent heat of fusion (1000 J·kg^{-1})
- Case Ib with a higher value of latent heat of fusion ($1.8 \cdot 10^6$ J·kg^{-1}) which matches this of silicon.

Only one case is examined for truncated cone, Case II, which uses the same input parameters as Case Ia, i.e. material properties as well as height and absorber surface. The parameters used for the verification cases are listed in Table 1.

During verification process, constant k and ρ values have been assumed, for simplicity reasons. However, at a next step of the simulation, different values have been considered for the PCM properties at its solid and liquid phases. A constant input temperature of 100°C has been assumed at the absorber surface for the melting case. Furthermore, a uniform initial temperature of 20°C along the length of the vessel is considered. For the discretization, the number of nodes used were n=202 and the number of time intervals was 20000.

2.5.2. Parametric investigation (PCM properties, vessel design)

During the melting process, heat is considered to originate from the vessel upper part (absorber) and, thus, a constant temperature is set there. Furthermore, some cases with different dimensions of the cylindrical geometry have been investigated, keeping the same volume in each case. From this investigation, the geometry with the optimal shape and size is highlighted and selected also for the solidification cases. The boundary conditions assigned for the 1D

**Table 6**
List of cases simulated, during the PCM solidification.

Test Case	Sensitivity analysis Parameters	Range
1	Difference between k_l and k_s, Δk	50%-100%-200%-300%
2	Thermal conductivity of liquid, k_l	50%-100%-200%-300%
3	Specific heat capacity, c_p	50%-100%-200%-300%
4	Latent heat of fusion, L	60%-80%-100%-120%-140%
5	Density, ρ	90%-100%-110%-120%
6	Initial upper surface temperature, T_1	90%-100%-110%-120%

Table 7
List of cases simulated, during the PCM melting.

Test Case	Sensitivity analysis Parameters	Range
1	Thermal conductivity of liquid, k	25%-50%-100%-125%-150%
2	Specific heat capacity, c_p	90%-95%-100%-105%-110%
3	Latent heat of fusion, L	80%-90%-100%-110%-120%
4	Absorber surface temperature, T_{abs}	90%-95%-100%-105%-110%
5	Initial temperature, T_{in}	90%-95%-100%-105%-110%

model during silicon solidification are presented in Table 2, and during silicon melting in Table 3.

The PCM-gas thermophysical properties are listed in Table 4. The silicon properties are retrieved from the literature [48]. A small melting interval of 2K (1679-1681) is used, for numerical reasons, in order to avoid jumps in PCM properties, during their transition from solid to liquid phase and vice versa. In reality, in pure metals, like pure silicon, there exists no 'mushy' zone, since their phase-change transition occurs in a single temperature point [49]. However, in several substances, such as metal alloys or paraffins, a mushy region exists, because the phase change in these substances
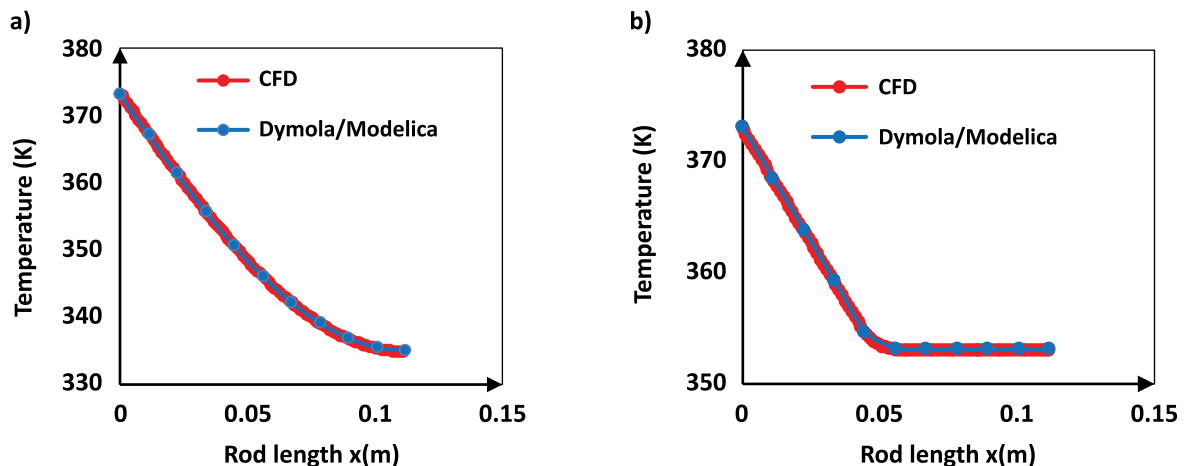
Fig. 5. Temperature profile along the cylinder length for a) Case Ia at time instant t=0.26s and b) Case Ib at time instant t=5.45s.
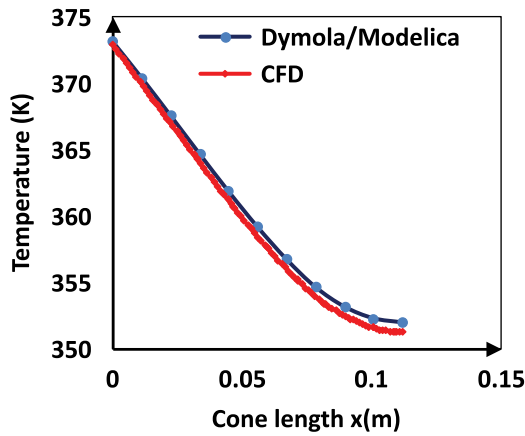
Fig. 6. Temperature profile along the truncated cone length at time instant t=0.32s.

Fig. 8. Heat input through the absorber surface for each of the cases.

occurs in a temperature interval. The extent of this interval and subsequently of the mushy region is variable, depending on the PCM.

For the PCM solidification modelling, the initial temperatures at the emitter surface and at the upper part of the tank are set equal to 1680 K and 1960 K, respectively. For the rest of the domain a linear interpolation of these two values is used to patch the temperature profile. For the PCM melting process, initially a uniform temperature is patched in the whole domain, lower than the PCM melting point and equal to 1543.75 K. Table 5 summarizes the cases simulated with different dimensions for the PCM melting case by means of the 1D model.

A sensitivity analysis both for the melting and the solidification phase of the PCM has also been performed based on key parame-
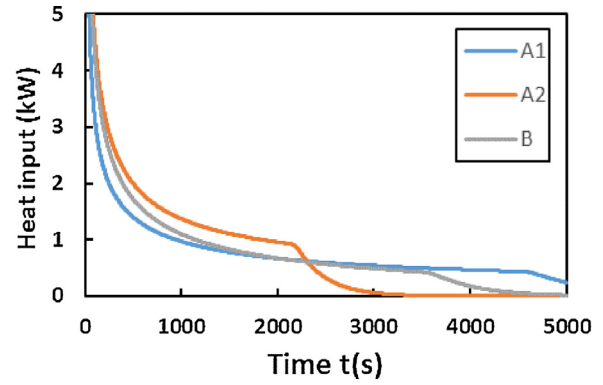
ters such as material properties (thermal conductivity, specific heat capacity, density, latent heat of fusion) and other operating conditions (initial temperature etc.). The purpose of this analysis is to cover to some extent the possible variation of these parameters in different materials [50–53].

For the following sensitivity analysis, Case A2 with the lower height has been selected as a reference case (100%), both for solidification and melting in the 1D model. Table 6 summarizes the cases tested, during the sensitivity analysis for the solidification case, while Table 7 summarizes the cases tested, during the sensitivity analysis for the melting.

2.5.3. Integration of heat storage block on building level

The PV capacity and PCM heat storage block is upscaled and integrated on a building level in order to cover the electric and heat demand of a building for a 24 h period. The capacity of the upscaled PV is 15kW. The capacity of the upscaled heat storage is
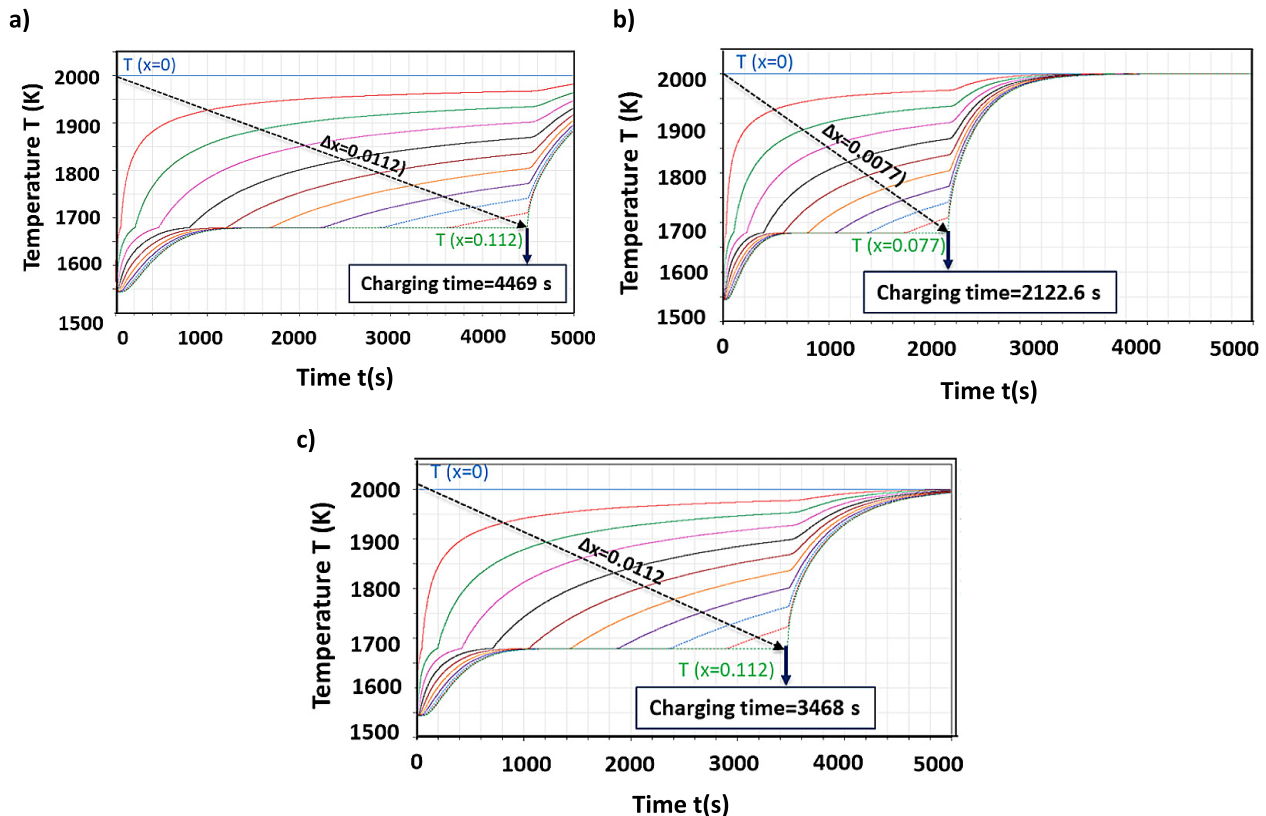

Fig. 7. Temperature as a function of time at various points along the shape length for a) Case A1, b) Case A2, c) Case B.
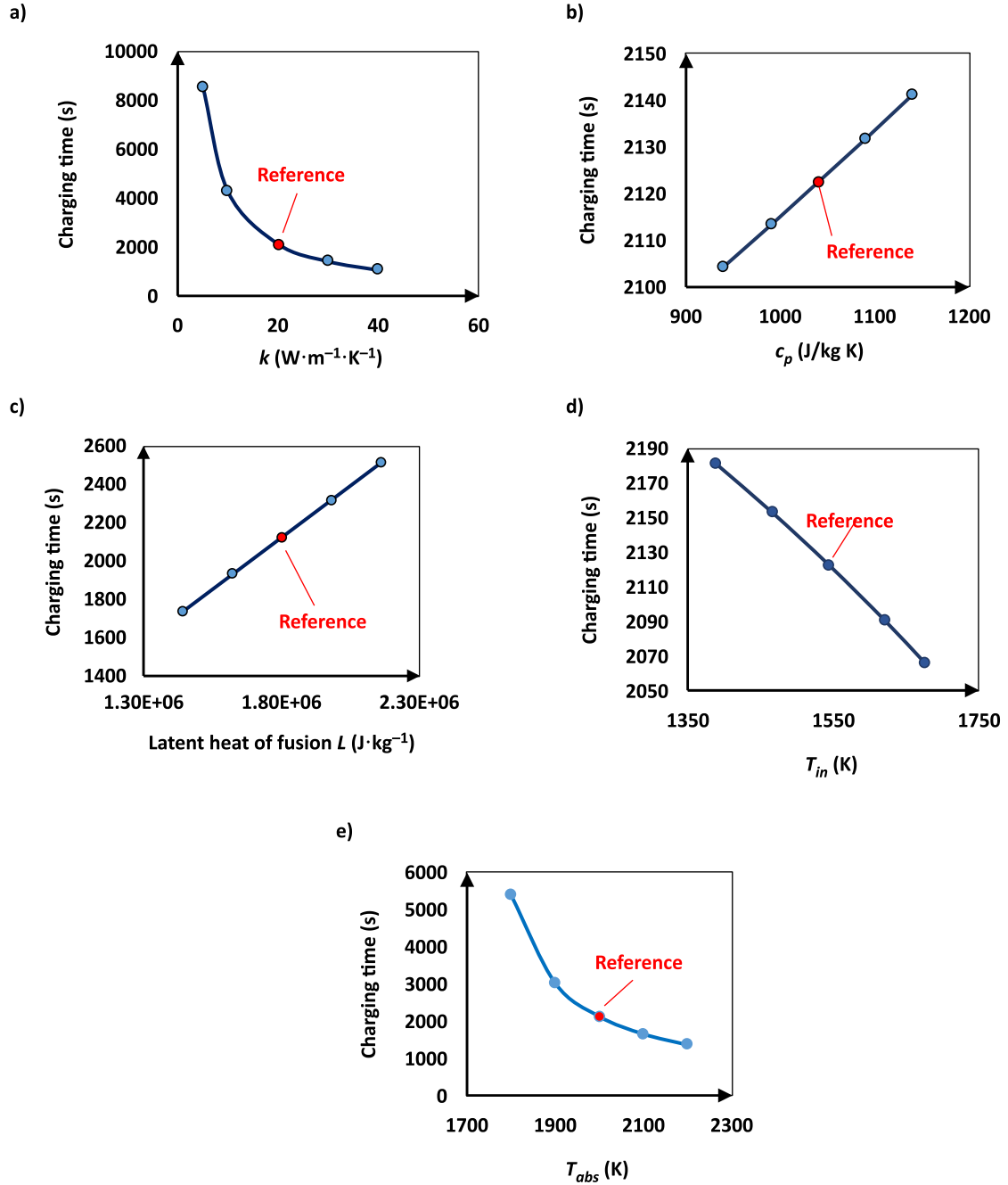
Fig. 9. Sensitivity analysis parameters during melting: a) thermal conductivity, b) specific heat capacity, c) latent heat of fusion, d) initial temperature of PCM and e) absorber temperature.

40kWh and the new dimensions are H=0.2661 m, A_{abs}=0.1291 m^2 which keeps the same ratio of cylinder height to diameter (H/D) with Case A2, but with a volume approximately 40 times larger. The capacity is upscaled at a reasonable level, in order to demonstrate a potential scenario for a realistic application of the integration based on the given residential needs and PV production. In this scenario, the PV covers as much of the electricity demand can be covered directly and the excess is fed to the heat storage, to be used whenever needed. An optimization of the capacity and dimensions will be performed in future work.

The heat storage block is charged, when there is available power coming from the PV system, and, discharged, when there is a corresponding heat and/or electricity demand. In this assess-

ment, two different strategies for discharging are investigated, i.e. a) covering heat demand as a priority or b) covering electricity demand as a priority. In the first one, the heat load is served as a priority, which means that at every moment the power output from the heat storage system -which must be within the limit which is defined by Eq. (8)- is set in that way so that the share which corresponds to the produced heat, can cover as much share from the heat demand as possible. The remaining extracted energy is converted to electricity at the specified ratio, with the target to cover as much of the electric demand as possible. On the other hand, in the second case, the electricity demand is served as a priority. Similarly, the power output from the heat storage system is set in that way so that the share which corresponds to the produced electric-
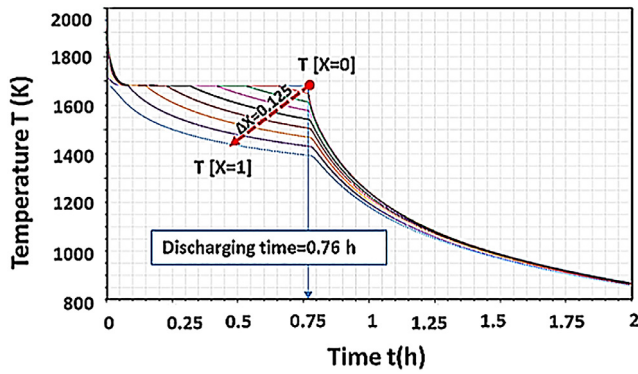
Fig. 10. Temperature as a function of time at various points along the cylinder length.
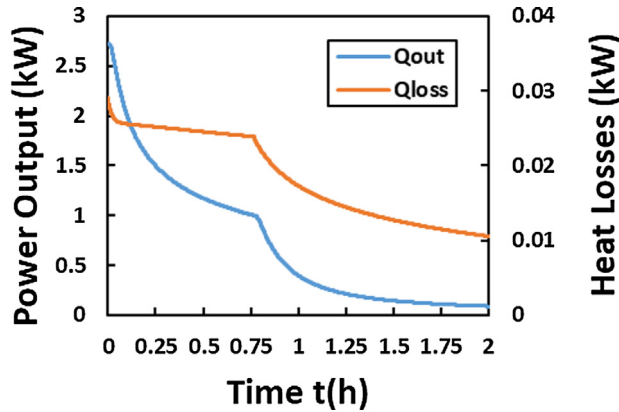

Fig. 11. Power output and heat losses of the cylinder at the solidification phase.

ity can cover as much share from the electricity demand as possible and the remaining is converted to heat at the specified ratio.

The charging and discharging strategy is applied by a separate Dymola model as seen in Fig. 2b), which simulates a charge control unit. This unit outputs specific signals that control when the heat storage system enters or leaves a charging and/or discharging state. When the heat storage system is neither at a charging nor at a discharging state, there is a stand-by mode in which the heat is neither absorbed nor emitted and just stored in the form of latent heat.

3. Results and discussion

The simulation results from the verification and sensitivity analysis are presented in the following subsections. The resulting heat and electricity production per hour for covering the corresponding demand of a 24-h period are also presented. Finally, the percentage of heat and electricity demand covered from RES has also been calculated.

3.1. 1D model verification

The verification of the melting cases showed good agreement between the 1D Dymola Model and the CFD model, which implies great precision of the developed 1D model. Negligible deviations in the temperature profile are observed in all cases, as seen in Fig. 5a and b for the cylinder cases Ia and Ib correspondingly and in Fig. 6 for the truncated cone case II, which depict the temperature profile along the shape length for selected time instants. This gives a reliability on the final objective to conduct different numerical tests both with a low computational cost (computational time in the order of 1-2 min) and a reasonable accuracy.

Table 8
Total charging time of the PCM for each of the cases.

Shape	Case	Charging time
Cylinder	Case Ia	0.47 s
	Case Ib	28.96 s
Truncated cone	Case II	0.36 s

Table 9
Total charging time of the PCM for each of the cases.

Shape	Case	Charging time	Relative difference (%)
Cylinder	Case A1	74.48 min	-
	Case A2	35.38 min	−52.5%
Truncated cone	Case B	57.80 min	−22.4%

The total charging time has also been verified against the CFD model results, and is shown in Table 8 as recorded/calculated for each case.

The verification of the 1D model has also been performed for the solidification case, based on a comparison of discharging time with previous results of the CFD model. The results showed that discharging time for the 1D model was 0.76 h and for an equivalent case simulated with a CFD model, it was recorded to be ~0.72 h, showing also a good agreement, with a relative difference equal to ~5 %, for the solidification case.

Such a good agreement with the more advanced CFD model confirms the aforementioned assumption that in the present cases studied, conduction is the major driving force in the PCM melting and solidification phases. Natural convection does not influence heat transfer due to the heat source location, which is on top of the vessel and the imposed boundary condition for discharging at the bottom. Therefore, taking also into account the high value of thermal conductivity, which is almost an order of magnitude higher than that of the conventional molten salt based PCMs, it is justified that conduction along the length of the vessel predominates during both the melting phase and the solidification phase, limiting the phenomenon of heat transfer mainly in the axial direction. In other configurations such as heating from the sidewalls, it is expected that natural convection would have a much greater role, resulting in higher rate of melting.

3.2. 1D model application to UHT LHTES block

3.2.1. Melting phase
3.2.1.1. Reference case. Fig. 7 presents the temperature as a function of time at various points along the PCM vessel length for each of the melting cases listed previously in Table 5. The space between each point selected is Δx.

The charging time, in minutes, for each of the above cases is presented in Table 9.

From these results, it is obvious that Case A2 is the case with the faster charging time, and it is used as a reference for the following sensitivity analysis both for the melting and solidification cases. The relative difference between case A2 and A1 is −52.50% and between case B and A1 is −22.40%. This relative difference is owed to the different geometry of each case. In particular, in Case A2 the vessel has a lower height compared to Case A1, but the same volume, which also means a higher absorber surface. In Case B, the cone has the same volume and height with the cylinder in Case A1, but also a higher absorber surface which justifies the shorter charging time compared to case A1 but longer compared to A2 due to the difference in height. The dependence of charging time on vessel length is proven as well in other previous works [25].
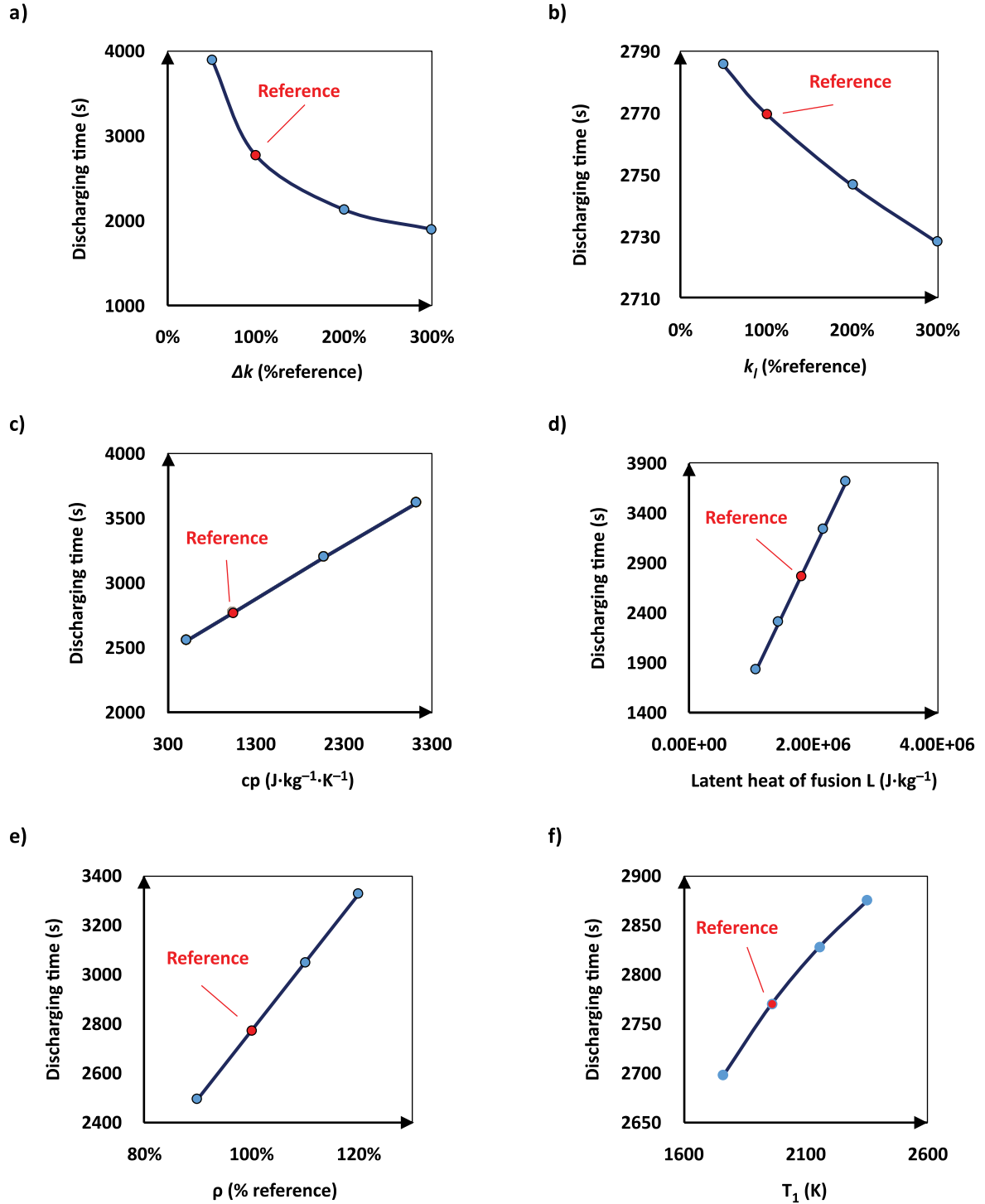
Fig. 12. Sensitivity analysis parameters during solidification: a) difference between k_l and k_s, b) thermal conductivity of liquid, c) specific heat capacity, d) latent heat of fusion, e) density and f) initial temperature of upper surface.

The heat input entering the vessel through the absorber surface for each of the cases is present in Fig. 8. The heat flux is initially very high when the temperature difference between the absorber and the rest of the PCM is extreme. However, it drops sharply and tends to stabilize as the temperature difference is tempered, up to the point when the PCM is fully charged and then the heat input begins to drop again as the temperature tends to equalize. There is no heat loss considered in these cases, as previously mentioned in Table 3. Based on this heat flux, the total energy stored in the UHT-TES during charging time has been calculated. Both in case A1

and A2, the total energy stored adds up to approx. 1.13 kWh when fully charged, while in case B the total energy corresponds to 1.16 kWh.

3.2.1.2. Sensitivity analysis. The results of the sensitivity analysis for the parameters listed previously in Table 7 are presented in Fig. 9. The sensitivity analysis showed that the charging time increases when increasing c_p and L and decreases when increasing k, T_{abs} and T_{in}. While the dependence on c_p, L and T_{in} is linear, a higher sensitivity of the charging time for lower values of
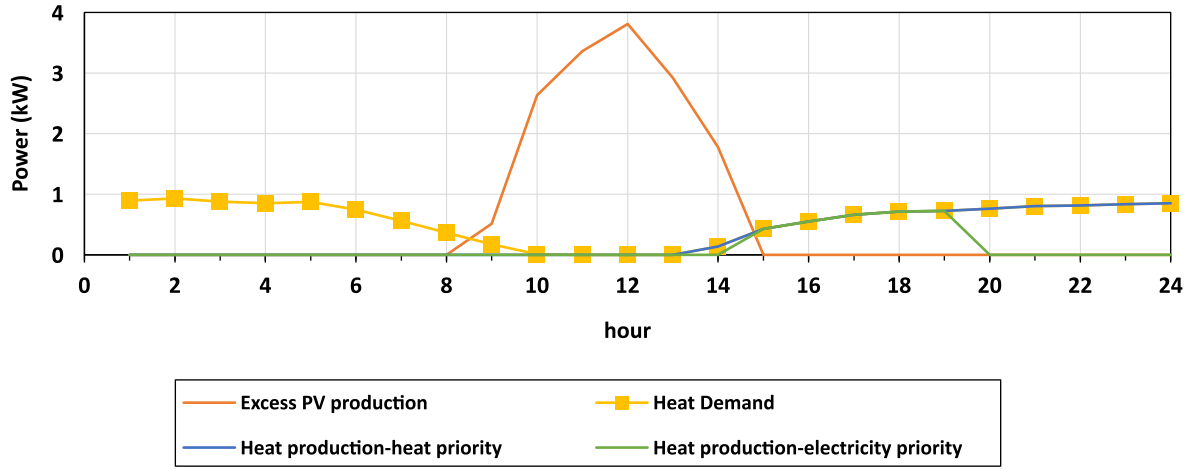
Fig. 13. PV production, heat demand and heat production with heat and electricity priority strategy.
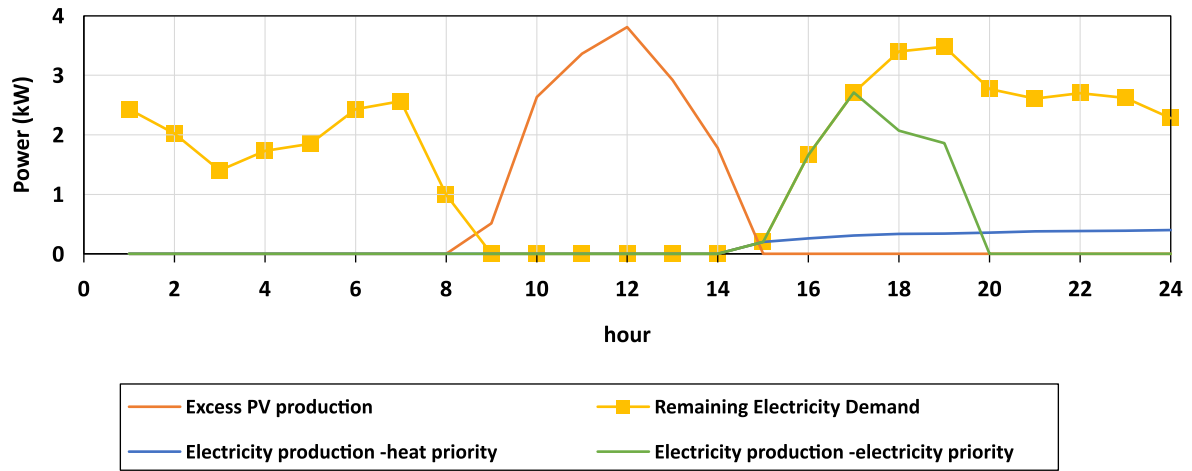

Fig. 14. PV production, electricity demand and electricity production with heat and electricity priority strategy.

k and T_{abs} was revealed. From the validation cases, it has also been shown that lower density of the PCM means faster charging times.

These sensitivity analyses also reveal that a 100% increase of k compared to the reference case leads to a 50% decrease of charging time, a 10% increase in c_p leads to a 0.9% increase of charging time, a 20% increase in latent heat leads to an 18.22% increase of charging time, an 8.5% increase in initial temperature T_{in} leads to a 2.7% decrease of charging time and a 10% increase in absorber temperature T_{abs} leads to a 36% decrease of charging time.

3.2.2. Solidification phase
3.2.2.1. Reference case.
The temperature as a function of time at various points along the cylinder length for the solidification case is presented in Fig. 10. Discharging time has been calculated to be 0.76 h or 45.6 min. This is used as a reference for the following sensitivity analysis.

The power output according to Eq. (8) and the heat losses of the cylinder according to Eq. (9) are presented in Fig. 11. The power output does not remain constant but has a descending form according to the temperature of the emitter which is decreasing with time. The heat losses from the sidewalls, which are also calculated, are very small compared to the output due to the very

high thermal resistance (R=1.88) considered and do not exceed 30 W at all times.

3.2.2.2. Sensitivity analysis.
The results of the sensitivity analysis for the parameters listed in Table 6 are presented in Fig. 12. The sensitivity analysis shows that discharging time is increasing with c_p, L, ρ and T_1 and decreasing with Δk, and k_l. These results are expected, since an increase in any of the former parameters (c_p, L, ρ and T_1) would imply an increase in the stored energy within the PCM, and therefore more time would be required for full discharge of this energy. On the other hand, an increase in any of the latter parameters (Δk and k_l) which are associated with thermal conductivity would reduce the difficulty of heat being transferred from the PCM to the emitter surface. Overall, it can be observed that the dependence on c_p, L and ρ is linear, and on T_1 and k_l is almost linear. A non-linear dependency on Δk is observed, revealing a higher sensitivity for lower values of Δk and greater impact on the discharging time.

The sensitivity analysis results also reveal indicatively that a 100% increase of Δk compared to the reference case leads to a 22.9% decrease of discharging time, a 100% increase in k_l leads to a 0.8% decrease of discharging time, a 100% increase in c_p leads to a 15.3% increase of discharging time, a 20% increase in latent heat leads to a 16.9% increase of discharging time, a 20% increase in ρ

Table 10
Percentage of heat and electricity demand covered for each strategy.

	heat priority strategy	electricity priority strategy
Heat (%)	53.7%	22.7%
Electricity (%)	8.4%	21.3%

leads to a 20% decrease of discharging time and a 20% increase in temperature T_1 leads to a 3.8% increase of discharging time.

3.3. Integration of heat storage block on building level

Fig. 13 shows the PV production, the heat demand and the heat production for each of the two heat and the electricity priority strategies and Fig. 14 shows the corresponding electricity demand and electricity production according to them, respectively, for a 24 h period of a typical day in winter, at the 20th of January.

With the heat priority strategy, the heat demand can be fully covered from 13:00 to the end of the 24 h period. A full coverage of electricity is also achieved from 14:00 to 15:00 and partially for the rest of the 24 hour period. On the other hand, with the electricity priority strategy, the full coverage of electricity demand is achieved from 14:00 to 17:00. A much higher part of the electricity demand is covered than in the heat priority strategy, but in this case the full coverage of heat demand is limited between 14:00 and 19:00. The total percentage of heat and electricity demand covered from RES during the 24 h period for both strategies –heat priority and electricity priority- has been calculated and presented in Table 10.

It is observed that the percentage of heat covered from RES even with the heat priority strategy, which adds up to 53.7 %, is comparable to the results from other studies such as the work of Belmonte et. al [15] where a TES system using PCM achieves solar contributions of about 50% of house heating requirements of a single-family house in corresponding locations of Southern Europe with mild winter conditions, such as Madrid and Barcelona. A more detailed yearly base analysis on the proposed energy system at residential level and a comparison with other heat storage options is suggested for future work.

4. Conclusions

An extensive numerical analysis was carried out, by means of a 1D model in Dymola, to evaluate the performance of the proposed latent heat thermal energy storage system. The main target of this analysis is to evaluate the thermal performance of the heat storage block under varying PCM properties and operating conditions. The 1D model was verified against the CFD results both for melting and solidification. A good agreement of results was observed, especially in the case of cylindrical geometry. Furthermore, it was shown that the optimized shape for melting is a cylinder with a lower height which was also selected for the solidification cases. Next, the sensitivity analysis showed a dependence of charging and discharging time on varying parameters such as PCM properties and initial temperature profile.

Finally, a potential domestic application of the latent heat thermal energy system was investigated. Modelling of the integrated heat storage system at a building level in order to cover the electric and thermal needs of a typical household has shown that with a typical size of 15 kW$_p$ PV system and a 40kWh heat storage capacity, a high percentage, over 50% of the heating demands can be met while covering almost 8% of the electricity demands when a heat priority strategy is followed. On the other hand, a higher percentage of electricity demand is covered (~21%) when an electricity priority strategy is followed, with a respectable percentage of heating demand (~23%) covered at the same time.

Unlike other energy storage technologies, the proposed LHTES-TIPV system has the ability to provide both electricity and heat, making it appealing for application at residential buildings. As the energy analysis of a UHT LHTES system operating at domestic level has not been studied extensively in the past, new investigations should follow to evaluate the potential feasibility of this novel concept. A more detailed analysis on the system design should be performed, addressing technical issues such as the effective heat transfer from the TIPV to the hot water circuit, the heat losses mitigation and the selection of the appropriate materials with improved properties under the specified demanding conditions ($>1000°C$). Additionally, more studies for a detailed cost engineering on the storage system and the conditions that make it economically feasible is suggested followed by comparative assessments with other competitive storage technologies.

In conclusion, the LHTES-TIPV concept has strong potential for domestic application that is worth further investigation.

Declaration of Competing Interest

The authors declare that they have no known competing financial interests or personal relationships that could have appeared to influence the work reported in this paper.

CRediT authorship contribution statement

I. Violidakis: Conceptualization, Methodology, Writing - original draft. **M. Zeneli:** Methodology, Writing - review & editing. **K. Atsonios:** Supervision, Writing - review & editing. **G. Strotos:** Writing - review & editing. **N. Nikolopoulos:** Supervision, Writing - review & editing. **S. Karellas:** Writing - review & editing.

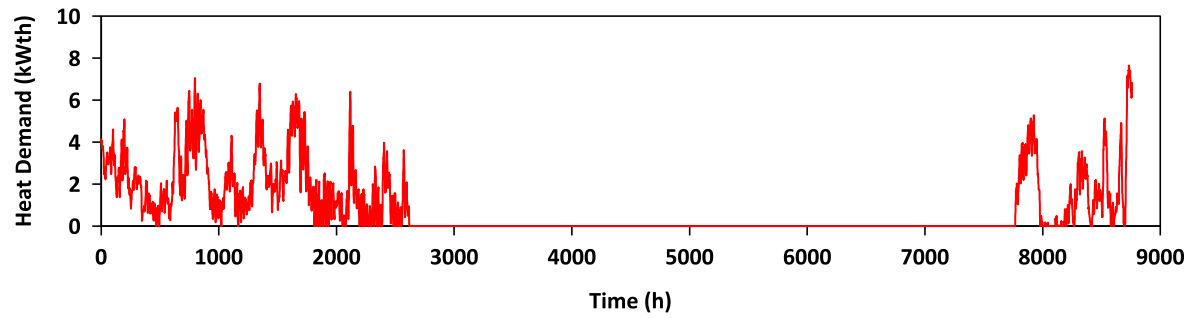### Annex

Figs. 15–19.

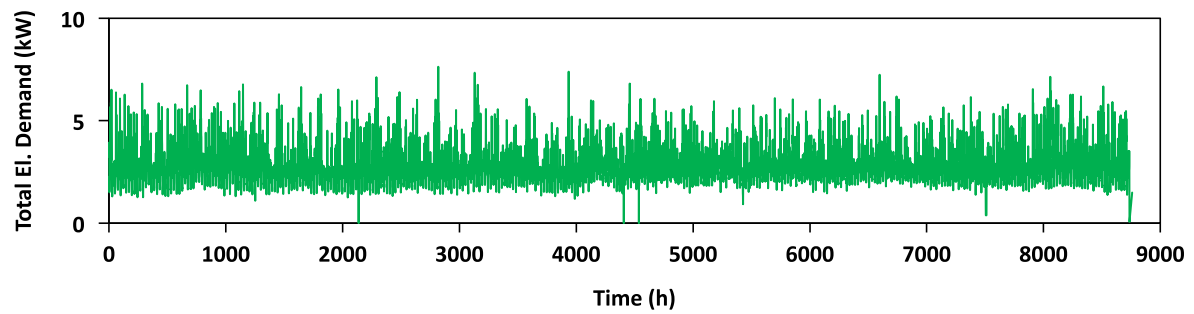**Fig. 15.** Heat demand throughout a year.

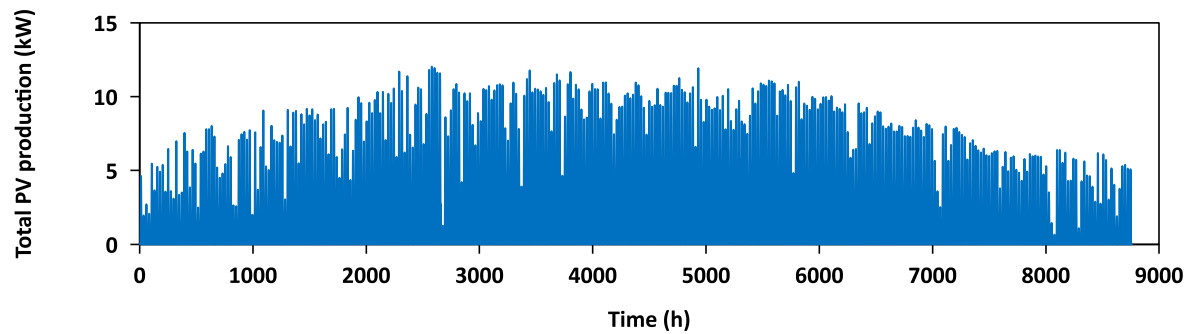**Fig. 16.** Electricity demand throughout a year.

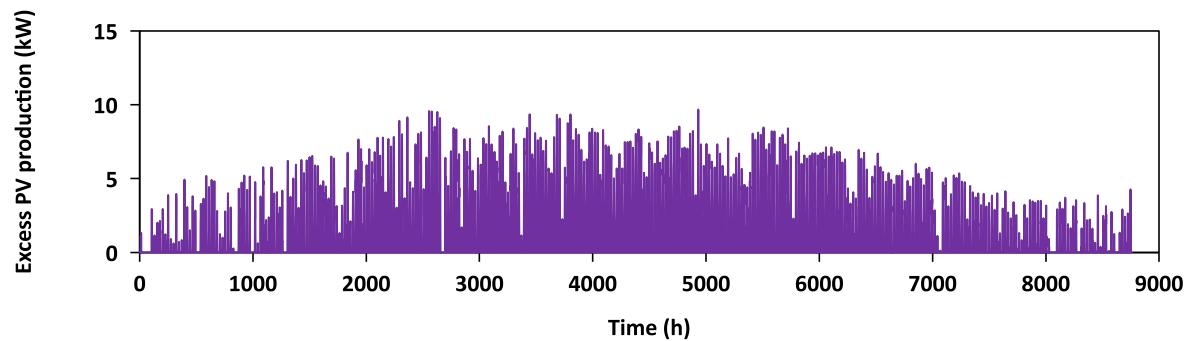**Fig. 17.** Typical electricity power production from a PV system installed in S. Europe throughout a year.

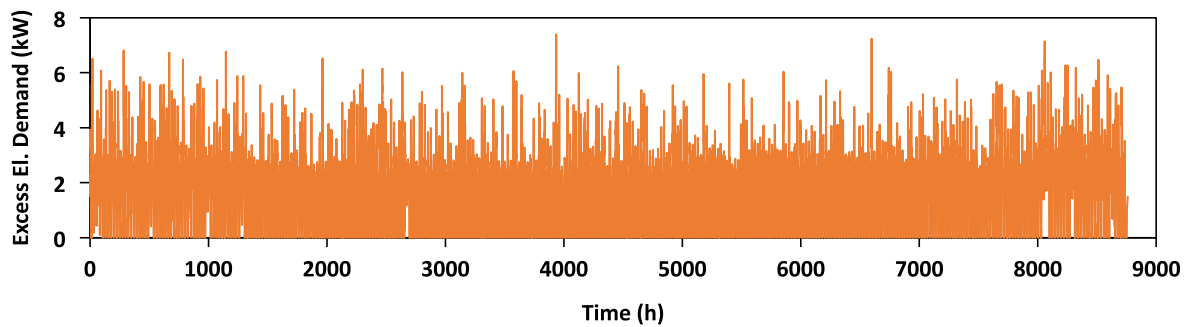**Fig. 18.** Excess electricity power production from a PV system.

Fig. 19. Remaining electricity demand throughout a year.

References

[1] J.S.f.P. Report, Energy Consumption and Energy Efficiency Trends in the EU-28 2000-2015, in, 2018.

[2] I.E. Agency, Key World Energy Statistics, in, Paris, France, 2017.

[3] J.C. Solano, L. Olivieri, E. Caamaño-Martín, Assessing the potential of PV hybrid systems to cover HVAC loads in a grid-connected residential building through intelligent control, Appl. Energy 206 (2017) 249–266.

[4] D. Mugnier, R. Fedrizzi, R. Thygesen, T. Selke, New generation solar cooling and heating systems with IEA SHC Task 53: overview and first results, Energy Procedia 70 (2015) 470–473.

[5] U. Eicker, A. Colmenar-Santos, L. Teran, M. Cotrado, D. Borge-Diez, Economic evaluation of solar thermal and photovoltaic cooling systems through simulation in different climatic conditions: an analysis in three different cities in Europe, Energy Build. 70 (2014) 207–223.

[6] N. Hartmann, C. Glueck, F.P. Schmidt, Solar cooling for small office buildings: Comparison of solar thermal and photovoltaic options for two different European climates, Renewable Energy 36 (5) (2011) 1329–1338.

[7] Y. Li, G. Zhang, G.Z. Lv, A.N. Zhang, R.Z. Wang, Performance study of a solar photovoltaic air conditioner in the hot summer and cold winter zone, Sol. Energy 117 (2015) 167–179.

[8] De B.R, R Coninck, B Verbruggen, J Driesen, D Saelens, L. Helsen, Modelling and simulation of a grid connected photovoltaic heat pump system with thermal energy storage using Modelica,, in: 8th Int Conf Syst Simul Build, 2010, pp. 1–21. 2010.

[9] E.A.f.S.o.E. (EASE), in: Thermal Storage Position Paper, Brussels, July 2017, p. 13.

[10] I. Dincer, M. Rosen, Thermal Energy Storage: Systems and Application, 2011.

[11] R. Waser, F. Ghani, S. Maranda, T.S. O'Donovan, P. Schuetz, M. Zaglio, J. Worlitschek, Fast and experimentally validated model of a latent thermal energy storage device for system level simulations, Appl. Energy 231 (2018) 116–126.

[12] K. Cellat, B. Beyhan, Y. Konuklu, C. Dündar, O. Karahan, C. Güngör, H. Paksoy, 2 years of monitoring results from passive solar energy storage in test cabins with phase change materials, Sol. Energy (2019).

[13] D.J. Malan, R.T. Dobson, F. Dinter, Solar thermal energy storage in power generation using phase change material with heat pipes and fins to enhance heat transfer, Energy Procedia 69 (2015) 925–936.

[14] B. Grange, C. Dalet, Q. Falcoz, A. Ferrière, G. Flamant, Impact of thermal energy storage integration on the performance of a hybrid solar gas-turbine power plant, Appl. Therm. Eng. 105 (2016) 266–275.

[15] J.F. Belmonte, M.A. Izquierdo-Barrientos, A.E. Molina, J.A. Almendros-Ibáñez, Air-based solar systems for building heating with PCM fluidized bed energy storage, Energy Build. 130 (2016) 150–165.

[16] M.A. Izquierdo-Barrientos, C. Sobrino, J.A. Almendros-Ibáñez, Energy storage with PCM in fluidized beds: Modeling and experiments, Chem. Eng. J. 264 (2015) 497–505.

[17] M. Parsazadeh, X. Duan, Numerical and statistical study on melting of nanoparticle enhanced phase change material in a shell-and-tube thermal energy storage system, Appl. Therm. Eng. 111 (2017) 950–960.

[18] K. Kant, A. Shukla, A. Sharma, Performance evaluation of fatty acids as phase change material for thermal energy storage, J. Energy Storage 6 (2016) 153–162.

[19] P. Lamberg, R. Lehtiniemi, A.-M. Henell, Numerical and experimental investigation of melting and freezing processes in phase change material storage, Int. J. Therm. Sci. 43 (3) (2004) 277–287.

[20] A.R. Archibold, J. Gonzalez-Aguilar, M.M. Rahman, D. Yogi Goswami, M. Romero, E.K. Stefanakos, The melting process of storage materials with relatively high phase change temperatures in partially filled spherical shells, Appl. Energy 116 (2014) 243–252.

[21] H. Mehling, L.F. Cabeza, Heat and Cold Storage with PCM, Springer, 2008.

[22] Y.B. Tao, Y.L. He, Numerical study on thermal energy storage performance of phase change material under non-steady-state inlet boundary, Appl. Energy 88 (11) (2011) 4172–4179.

[23] Z. Wang, H. Wang, X. Li, D. Wang, Q. Zhang, G. Chen, Z. Ren, Aluminum and silicon based phase change materials for high capacity thermal energy storage, Appl. Therm. Eng. 89 (2015) 204–208.

[24] A. Datas, A. Ramos, A. Martí, C. del Cañizo, A. Luque, Ultra high temperature latent heat energy storage and thermophotovoltaic energy conversion, Energy 107 (2016) 542–549.

[25] A. Datas, M. Zeneli, C. del Cañizo, I. Malgarinos, A. Nikolopoulos, N. Nikolopoulos, S. Karellas, A. Martí, Molten silicon storage of concentrated solar power with integrated thermophotovoltaic energy conversion, AIP Conf. Proc. 2033 (1) (2018) 090005.

[26] A. Datas, A.B. Cristobal, C. del Cañizo, E. Antolín, M. Beaughon, N. Nikolopoulos, A. Nikolopoulos, M. Zeneli, N. Sobczak, W. Polkowski, M. Tangstad, J. Safarian, D.M. Trucchi, A. Bellucci, M. Girolami, R. Marx, D. Bestenlehner, S. Lang, A. Vitulano, G. Sabbatella, A. Martí, AMADEUS, Next generation materials and solid state devices for ultra high temperature energy storage and conversion, AIP Conf. Proc. 2033 (1) (2018) 170004.

[27] M.R. Reid, D.B. Scharfe, R.N. Webb, Computational evaluation of a latent heat energy storage system, Sol. Energy 95 (2013) 99–105.

[28] W. Chan, R. Huang, C. Wang, J. Kassakian, J. Joannopoulos, I. Celanovic, Modeling low-bandgap thermophotovoltaic diodes for high-efficiency portable power generators, Sol. Energy Mater. Sol. Cells 94 (3) (2010) 509–514.

[29] G.N. Hatsopoulos, E.P. Gyftopoulos, Thermionic energy conversion. Volume I. Processes and devices, Massachusetts Institute of Technology Press, Cambridge, MAUnited States, 1973 Originating Research Org. not identified.

[30] W. Polkowski, N. Sobczak, G. Bruzda, A. Kudyba, R. Nowak, A. Polkowska, I. Krzak, A. Tchórz, D. Giuranno, Silicon-Boron Alloys as New Ultra-High Temperature Phase-Change Materials: Solid/Liquid State Interaction with the h-BN Composite, Silicon (2019).

[31] J. Jiao, B. Grorud, C. Sindland, J. Safarian, K. Tang, K. Sellevoll, M. Tangstad, The use of eutectic Fe-Si-B alloy as a phase change material in thermal energy storage systems, Materials 12 (2019) 2312.

[32] A. Datas, D.L. Chubb, A. Veeraragavan, Steady state analysis of a storage integrated solar thermophotovoltaic (SISTPV) system, Sol. Energy 96 (2013) 33–45.

[33] A. Veeraragavan, L. Montgomery, A. Datas, Night time performance of a storage integrated solar thermophotovoltaic (SISTPV) system, Sol. Energy 108 (2014) 377–389.

[34] M. Zeneli, I. Malgarinos, A. Nikolopoulos, N. Nikolopoulos, P. Grammelis, S. Karellas, E. Kakaras, Numerical simulation of a silicon-based latent heat thermal energy storage system operating at ultra-high temperatures, Appl. Energy 242 (2019) 837–853.

[35] V.R. Voller, P, C, A fixed grid numerical modelling methodology for convection-diffusion mushy region phase-change problems, Civil Environ. Geo- Eng. (1987).

[36] A. Datas, A. Ramos, C. del Cañizo, Techno-economic analysis of solar PV power-to-heat-to-power storage and trigeneration in the residential sector, Appl. Energy 256 (2019) 113935.

[37] A. Datas, A.B. Cristobal, C. del Cañizo, E. Antolín, M. Beaughon, N. Nikolopoulos, A. Nikolopoulos, M. Zeneli, N. Sobczak, W. Polkowski, M. Tangstad, J. Safarian, D.M. Trucchi, A. Bellucci, M. Girolami, R. Marx, D. Bestenlehner, S. Lang, A. Vitulano, G. Sabbatella, A. Martí, AMADEUS, Next generation materials and solid state devices for ultra high temperature energy storage and conversion, AIP Conf. Proc. 2033 (2018) 170004 170001-170010.

[38] M. Zeneli, A. Bellucci, G. Sabbatella, D.M. Trucchi, A. Nikolopoulos, N. Nikolopoulos, S. Karellas, E. Kakaras, Performance evaluation and optimization of the cooling system of a hybrid thermionic-photovoltaic converter, Energy Convers. Manage. (2020).

[39] Heating and cooling degree days, in, European Environment Agency (EEA), https://www.eea.europa.eu/data-and-maps/indicators/heating-degree-days-2 Jun 2019.

[40] TABULA WebTool, in, http://webtool.building-typology.eu/#bm, 10/2019.

[41] G. Hoogsteen, A. Molderink, J.L. Hurink, G.J.M. Smit, Generation of flexible domestic load profiles to evaluate Demand Side Management approaches, in: 2016 IEEE International Energy Conference (ENERGYCON), 2016, pp. 1–6.

[42] P.G. Kroeger, S. Ostrach, The solution of a two-dimensional freezing problem including convection effects in the liquid region, Int. J. Heat Mass Transfer 17 (10) (1974) 1191–1207.

[43] C. Lapadula, W.K. Mueller, Heat conduction with solidification and a convective boundary condition at the freezing front, Int. J. Heat Mass Transfer 9 (7) (1966) 702–704.

[44] N.S. Dhaidan, J.M. Khodadadi, Melting and convection of phase change materials in different shape containers: A review, Renewable Sustainable Energy Rev. 43 (2015) 449–477.

[45] M. Zeneli, A. Nikolopoulos, A. Datas, N. Nikolopoulos, S. Karellas, E. Kakaras, Study of heat losses during charge, discharge and storage period of a LHTES system operating at ultra-high temperatures, ECOS Conference, 2019.

[46] A. Datas, Hybrid thermionic-photovoltaic converter, Appl. Phys. Lett. 108 (14) (2016) 143503.

[47] E. Assis, L. Katsman, G. Ziskind, R. Letan, Numerical and experimental study of melting in a spherical shell, Int. J. Heat Mass Transfer 50 (9) (2007) 1790–1804.

[48] S. Basu, Crystalline Silicon - Properties and Uses, Web of Sciences, 2011.

[49] A.C. Reardon, Metallurgy for the Non-Metallurgist, second ed., 2011.

[50] S.S. Chandel, T. Agarwal, Review of current state of research on energy storage, toxicity, health hazards and commercialization of phase changing materials, Renewable Sustain. Energy Rev. 67 (2017) 581–596.

[51] H. Mehling, L.F. Cabeza, Phase change materials and their basic properties, in: H.Ö. Paksoy (Ed.), Thermal Energy Storage for Sustainable Energy Consumption, Springer, Netherlands, Dordrecht, 2007, pp. 257–277.

[52] X. Wang, J. Liu, Y. Zhang, H. Di, Y. Jiang, Experimental research on a kind of novel high temperature phase change storage heater, Energy Convers. Manage. 47 (15) (2006) 2211–2222.

[53] C.E. Birchenall, A.F. Riechman, Heat storage in eutectic alloys, Metall. Trans. A 11 (8) (1980) 1415–1420.